A controlled variable inductor for an LCC-S compensated Wireless Power Transfer system

Luigi Solimene
Dipartimento Energia
G. Ferraris (DENERG)
Politecnico di Torino
Torino, Italy
luigi.solimene@polito.it

Fabio Corti
Dipartimento di Ingegneria
Università di Perugia
Perugia, Italy
fabio.corti@unipg.it

Salvatore Musumeci
Dipartimento Energia
G. Ferraris (DENERG)
Politecnico di Torino
Torino, Italy
salvatore.musumeci@polito.it

Alberto Reatti
Dipartimento di Ingegneria
dell'informazione (DINFO)
Università di Firenze
Firenze, Italy
alberto.reatti@unifi.it

Carlo Stefano Ragusa
Dipartimento Energia
G. Ferraris (DENERG)
Politecnico di Torino
Torino, Italy
carlo.ragusa@polito.it

IECON 2022 – 48th Annual Conference of the IEEE Industrial Electronics Society | 978-1-6654-8025-3/22/$31.00 ©2022 IEEE | DOI: 10.1109/IECON49645.2022.9968576

***Abstract*—In this paper, an LCC-S compensated wireless power transfer system regulated by a variable inductor is presented. The inductance variation is performed by exploiting the magnetic material saturation of the inductor core, regulating the DC bias. The magnetic design of the controlled variable inductor is proposed. A low-cost auxiliary circuit for the regulation of the bias current is proposed, and the performance is evaluated. The effect of the inductance variation on the output power regulation and conversion efficiency are evaluated through an experimental setup.**

***Index Terms*—Wireless Power Transfer, LCC-S compensation, Magnetic control**

I. Introduction

Wireless Power Transfer (WPT) systems have several advantages with respect to wired solutions. The possibility of transferring power without a direct connection allows for avoiding the use of bulky cables [1]. In addition, the connection system represents one of the most critical elements due to the considerable numbers of charging required every day, which leads to wear. Thus, a wireless power transfer system results in a more robust product by removing the physical limitations of connectors, like mating cycles and corrosion of contacts. Thanks to this advantage and higher user comfort, WPT systems are nowadays used in several applications such as electric vehicles (EV) [1]–[4], mobile phones and electronic consumers [5], [6], unmanned aerial vehicles [7], and railways [8]. Depending on the physical principle used to perform the power transmission, WPT systems can be divided into two categories: Inductive Wireless Power Transfer (IWPT) [9] and Capacitive Wireless Power Transfer (CWPT) systems [10], [11]. An extensive comparison between these technologies has been proposed in [12]. Although CWPT can bring several advantages such as lower cost and weight, IWPT is nowadays the most matter technology able to allow the transmission at higher distances with higher efficiency [13]. In an IWPT system, the power is transferred by the magnetic coupling created between two coils. Several geometries have been proposed to increase the coupling and reduce the sensitivity to misalignment [14]. The distance between the coils depends on the applications. However, the coupling coefficient is usually low since an air gap separates the coils. Resonant compensation networks are usually adopted to increase the power transmission and minimise the reactive power due to the inductive nature of the coils [15], [16]. The compensation topology mainly adopted is the Series-Series (SS), obtained by adding two capacitors in series with the coils [17]. This topology acts as a current source on the secondary side and allows high transmission efficiency even at a low coupling coefficient [18]. Several other topologies have been proposed over the years to improve the performance of WPT [19]. As shown in [20], one of the most promising is the LCC-S, which acts as a voltage source. An advantage of this topology is the lower voltage/current stress across each component compared to the SS compensation. Several works are available in the literature regarding the LCC-S compensation. In [21], an EV wireless charging system able to charge with a CC/CV profile using an LCC-S compensation is presented. In [22], a design procedure for the LCC-S compensation optimised to make the system tolerant to misalignment is proposed. Another design procedure for the LCC-S compensation is presented in [23], where two fixed resonant frequencies are exploited to realise CC/CV under zero-phase angle conditions leading to zero voltage switching, thus reducing the switching loss. Most of the techniques available in the literature are focused on the component's optimisation to achieve high efficiency at a particular operating condition. As shown in [22], [23],

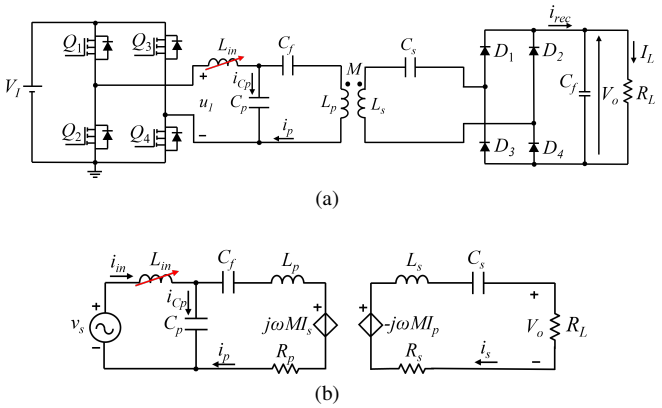

Fig. 1. (a) Circuit diagram of an LCC-S compensated WPT system. (b) Equivalent circuit of the first harmonic approximation of the system. $R_{\rm p}$ and $R_{\rm s}$ are the parasitic resistances of the primary and the secondary coils.

the output power regulation is obtained by changing the system topology through a power switch. Although it has been proven that this approach can reach acceptable DC-DC conversion efficiency, additional high-power components are required increasing the size and the cost of the system. This paper proposes a Magnetic Control (MC) strategy to regulate the output power of the LCC-S compensated WPT system. The MC, used for the LLC resonant converter, can be performed with a controlled variable inductor by adding an auxiliary winding where a DC current generates a DC bias magnetic flux density in the core, thus adjusting the magnetic permeability of the ferromagnetic material [24], [25]. The main advantage of the proposed technique is the continuous regulation of the inductance value between the unsaturated and the saturated value [26]. The paper is organised as follows. In Section II, the LCC-S compensation is presented. The expression of the transmission efficiency and output power are derived. Section III describes the magnetic design of the controlled variable inductor. Section IV presents and compares possible approaches to the DC current regulation. In Section V, an experimental setup is shown. Finally, in Section VI, the conclusions are derived.

II. LLC-S Resonant Compensation

A. Circuit description

The electric circuit of an LCC-S compensated WPT system is shown in Fig. 1a. The first harmonic approximation equivalent circuit is depicted in Fig. 1b, where $v_{\rm s}$ is the RMS value of the first harmonic of the square wave u_1. The relationships between capacitors and inductors, which allow to obtain the maximum power transfer and minimise the reactive power circulating in the system, are

$$L_{\rm s} = \frac{1}{\omega_0^2 C_{\rm s}}, \tag{1}$$

$$L_{\rm in} = \frac{1}{\omega_0^2 C_{\rm p}}, \tag{2}$$

$$L_{\rm in} = L_{\rm p} - \frac{1}{\omega_0^2 C_{\rm f}}. \tag{3}$$

Analysing the circuit shown in Fig. 1b, the output power can be defined as

$$P_0 = \frac{\omega^2 M^2 V_{\rm s}^2 R_{\rm L}}{R^2\omega^2 k_1^2 + k_2^2 k_5^2} \tag{4}$$

and the transmission efficiency is

$$\eta = \frac{\omega^2 M^2 R_{\rm L} C_{\rm f}}{R k_2 \left\{C_{\rm p} k_4 + k_5 (C_{\rm p} + C_{\rm f} k_6)\right\}}, \tag{5}$$

where

$$k_1 = L_{\rm in} + L_{\rm p} - \frac{1}{\omega^2 C_{\rm f}} + \frac{C_{\rm p} L_{\rm in}}{C_{\rm f}} - \omega^2 C_{\rm p} L_{\rm in} L_{\rm p}, \tag{6}$$

$$k_2 = \omega^2 M^2 + R_{\rm p} R, \tag{7}$$

$$R = R_{\rm L} + R_{\rm s}, \tag{8}$$

$$k_3 = 1 - \omega^2 L_{\rm p} C_{\rm f}, \tag{9}$$

$$k_4 = \omega^2 C_{\rm f}(L_{\rm in} + L_{\rm p}) + \omega^2 L_{\rm in} C_{\rm p} k_3 - 1, \tag{10}$$

$$k_5 = 1 - \omega^2 L_{\rm in} C_{\rm p}, \tag{11}$$

$$k_6 = 1 - \omega^2 L_{\rm p} C_{\rm p}. \tag{12}$$

M is the transformer coupling factor and $V_{\rm s}$ is the RMS value of the voltage $v_{\rm s}$. $R_{\rm p}$ and $R_{\rm s}$ are the parasitic resistances of the primary and the secondary coils, while $R_{\rm L}$ is the load resistance. When (1), (2) and (3) are verified, and the system operates in resonance, the previous expressions (4) and (5) can be simplified as

$$P_{\rm o} = \frac{\omega^4 C_{\rm f}^2 M^2 R_{\rm L} V_{\rm s}^2}{R^2(\omega^2 C_{\rm f} L_{\rm p} - 1)^2} \tag{13}$$

and

$$\eta = \frac{\omega^2 R_{\rm L} M^2}{R(\omega^2 M^2 + R R_{\rm p})} \tag{14}$$

B. Design procedure

Using (1)-(3) the system can be tuned to resonate at a particular operating frequency. The inductance values of the coils $L_{\rm p}$ and $L_{\rm s}$ are usually defined. (13) can be used to compute the $C_{\rm f}$ to achieve a desired output power $P_{\rm o}$ with a specific load resistance $R_{\rm L}$ as

$$C_{\rm f} = \frac{\omega L_{\rm p} + \sqrt{\omega^2(L_{\rm p}^2 - M^2 R_{\rm L} V_{\rm S}^2) - P_{\rm o} R^2 L_{\rm p}^2}}{\omega[P_{\rm o} R^2 L_{\rm p}^2 - M^2 R_{\rm L} V_{\rm S}^2 \omega^2]}. \tag{15}$$

The adopted transformer coupling factor M is the nominal value, considering no misalignment between the coils. Under this condition, the maximum power transfer is achieved, and the reactive power is zero. The input impedance is

$$Z_{\rm in} = R_{\rm in} + jX_{\rm in}, \tag{16}$$

where

$$R_{\rm in} = \frac{(R_{\rm L} + R_{\rm s})(\omega^2 C_{\rm f} L_{\rm p} - 1)^2}{\omega^2 C_{\rm f}^2(\omega^2 M^2 + R R_{\rm p})} \tag{17}$$

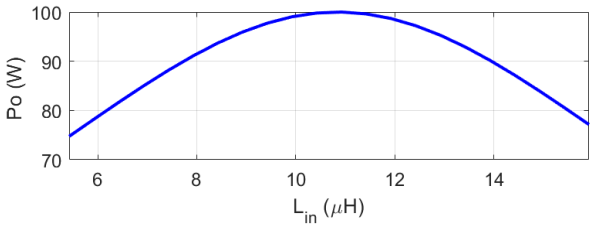

Fig. 2. Output power as a function of the input inductance value.

and

$$X_{\text{in}} = 0. \tag{18}$$

An experimental setup with the specification reported in Table I has been designed.

TABLE I
SYSTEM CONSTRAINTS

Parameter	Value	Description
f_{s}	85 kHz	Operating frequency
V_{I}	24 V	DC input voltage
P_{o}	100 W	Output power
k	0.36	Coupling coefficient
L_{p}	86.7 μH	Primary coil inductance
R_{p}	0.82 Ω	Primary coil parasitic resistance
L_{s}	93.4 μH	Secondary coil inductance
R_{s}	0.71 Ω	Secondary coil parasitic resistance
R_{L}	50 Ω	Load resistance

Using (1), (2), (3) and (15), the component values shown in Table II have been achieved. Using (4) and (5), the inductance L_{in} required for the output power and the transmission efficiency regulation can be computed. Fig. 2 represents the dependence of the output power on the input inductance value.

TABLE II
RESONANT COMPENSATION DESIGN

Parameter	Value	Description
C_{f}	46.2 nF	Filter capacitor
L_{in}	10.84 μH	Input inductor
C_{p}	323.3 nF	Primary capacitor
C_{s}	37.5 nF	Secondary capacitor

III. NOTES ON THE DESIGN OF THE CONTROLLED VARIABLE INDUCTOR

In this section, the procedure adopted for the design of a controlled variable inductor is described. The inductance regulation can be achieved by operating on the permeability of the magnetic core material. The differential permeability is defined as

$$\mu_{\text{d}} = \frac{1}{\mu_0}\frac{\text{d}B}{\text{d}H}. \tag{19}$$

Different magnetic field strength values lead the material to operate in three different regions of the magnetisation curve, from a linear region, where the differential permeability shows a near-constant profile, to a roll-off region, in which the permeability rapidly decreases, finally to a saturation region, where the minimum value of the differential permeability is obtained. The magnetisation curve and the differential permeability profile of the N87 Mn-Zn ferrite are shown in Fig. 3, where the different operating regions are highlighted [27].

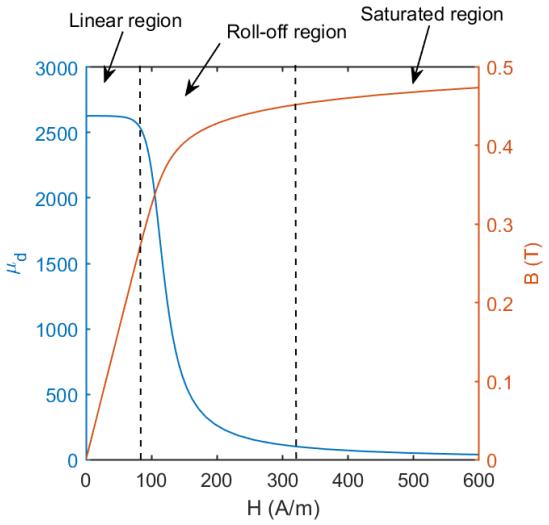

Fig. 3. Magnetisation curve of the N87 Mn-Zn ferrite, and the related differential permeability profile. The different operating regions of soft magnetic material are highlighted.

In this paper, the controlled variable inductor is realised on a double E core, with the main winding placed on the central leg and two auxiliary winding placed on the outer legs. The main winding is connected to the other parts of the LCC-S compensation network. The auxiliary windings, supplied by a suitable DC source, are connected in anti-series to force the DC magnetic flux path only in the outer legs of the double E cores. By controlling the direct current value in the auxiliary windings, the magnetic field strength in the ferromagnetic material of the outer legs is controlled. A concentrated air gap is adopted in the central leg to ensure the operation of the material in the linear region of the magnetisation curve. Fig. 4a represents the arrangement of the considered core geometry. The equivalent reluctance model represented in Fig. 4b is adopted to compute the differential inductance profile referred to the main winding.

The air gap reluctance and the ferromagnetic path reluctance of the central leg can be described as constant terms by

$$\mathcal{R}_{\text{fe,c}} = \frac{l_{\text{fe,c}}}{\mu_0\,\mu_{\text{fe,in}}\,S_{\text{fe,c}}}, \tag{20}$$

$$\mathcal{R}_{\text{g}} = \frac{l_{\text{g}}}{\mu_0\,S_{\text{g}}}, \tag{21}$$

while the reluctance of the outer leg can be described as

$$\mathcal{R}_{\text{fe,l}} = \frac{l_{\text{fe,l}}}{\mu_0\,\mu_{\text{fe,d}}\,S_{\text{fe,l}}}. \tag{22}$$

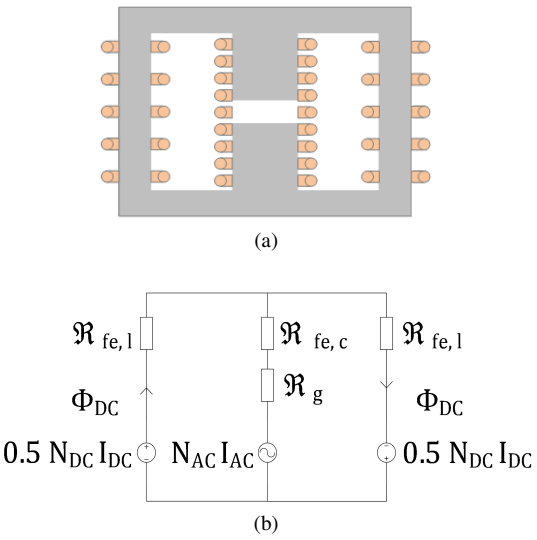

Fig. 4. Description of the core and winding configuration for the controlled variable inductor design. (a) Adopted double E core gapped configuration. (b) Equivalent reluctance circuit.

The permeability $\mu_{\mathrm{fe,in}}$ adopted in (20) is the initial permeability, while $\mu_{\mathrm{fe,d}}$ adopted in (22) is the differential permeability of the ferromagnetic material, that is a function of the DC magnetomotive force applied by the magnetising winding. The equivalent reluctance referred to the main winding is defined as

$$\mathcal{R}_{\mathrm{eq,d}} = \mathcal{R}_{\mathrm{fe,c}} + \mathcal{R}_{\mathrm{g}} + \mathcal{R}_{\mathrm{fe,l}}, \tag{23}$$

and thus, the differential inductance can be computed as

$$L_{\mathrm{d}} = \frac{N_{\mathrm{AC}}^2}{\mathcal{R}_{\mathrm{eq,d}}}. \tag{24}$$

To obtain the inductance profile suitable for the output power regulation of the designed LCC-S compensation topology, a N87 double E32/16/9 core is selected, with a 1 mm gap on the central leg, 10 turns on the main winding and 10 turns of the auxiliary winding, equally split on the outer legs. Fig. 5 represents the differential inductance profile of the designed variable inductor as a function of the magnetizing current of the auxiliary winding.

In Table III the electrical properties of the auxiliary winding are reported.

TABLE III
MEASURED DC WINDING CHARACTERISTICS

Parameter	Value	Description
L_{DC}	$114.4\ \mu$H	DC winding inductance
Q_{LDC}	96.4	Quality factor @ 10kHz
R_{DC}	$74.3\ \mathrm{m}\Omega$	Parasitic resistance

IV. DC CURRENT REGULATORS

One of the main critical aspects of magnetic control is the DC current regulation. This part describes an additional circuit that must not significantly increase the system cost and not affect system efficiency. This aspect has been already analysed in the literature. The regulation can be performed by a power MOSFET controlled by a linear or switching approach. As shown in Fig. 6a, the conventional voltage-controlled current source is realised. Extensive analyses of this linear control circuit have been presented in [28], [29].

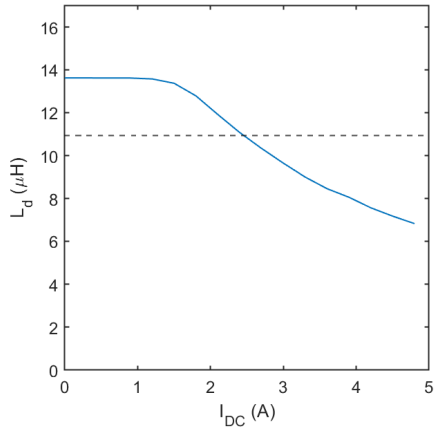

Fig. 5. Differential inductance profile of the proposed variable inductor, as a function of the current in the auxiliary windings.

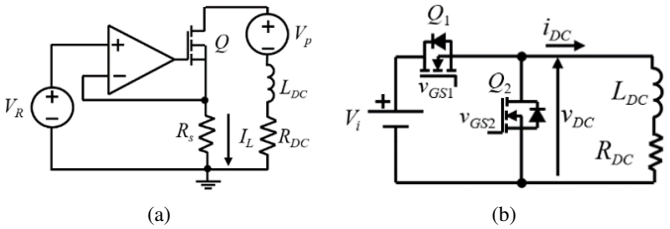

Fig. 6. Regulation of the magnetizing current in the auxiliary winding. (a) Linear regulation. (b) Switching regulation.

Although this approach allows reaching very stable and precise DC currents, it is usually characterised by high power losses on the resistor R_{S}, compromising the system efficiency. In particular, for high current values, a large amount of power is dissipated on the resistor R_{S}, requiring proper heat dissipation strategies and increasing the size of the auxiliary circuit. Another approach adopts a DC-DC switching power converter, as shown in Fig. 6b. The switching regulators operate with reduced power loss with respect to the linear regulator. This converter allows for increasing the power density of the auxiliary circuit, reducing the size and the cost. Since the load is the DC winding of the variable inductance ($R_{\mathrm{DC}} = 74.3\ \mathrm{m}\Omega$) and the current regulation is in the range $I_{\mathrm{DC}} = (0-3)$ A, the output voltage ($V_{\mathrm{DC}} = R_{\mathrm{DC}} \cdot I_{\mathrm{o}}$)) will be in the range $V_{\mathrm{DC}} = (0-223)$ mV. An input voltage $V_{\mathrm{i}} = 3.3$ V is chosen to avoid the operation with an extremely low duty cycle. The switching circuit can be realised using low current and low breakdown voltage MOSFETs operating in synchronous step-down converter topology [30]. A lower current ripple and a higher precise regulation can be achieved by increasing

the switching frequency, as represented in Fig. 7, where the transient response of the auxiliary winding is represented, with a target of $I_{\mathrm{DC}} = 1$ A is shown. For this reason, a switching frequency $f_{\mathrm{s}} = 500$ kHz is chosen. At this frequency value, GaN FETs are suitable for this application [31]. The simulated waveforms of Fig. 7 have been obtained using a model of the EPC2111 consisting of an enhancement-mode GaN power transistor.

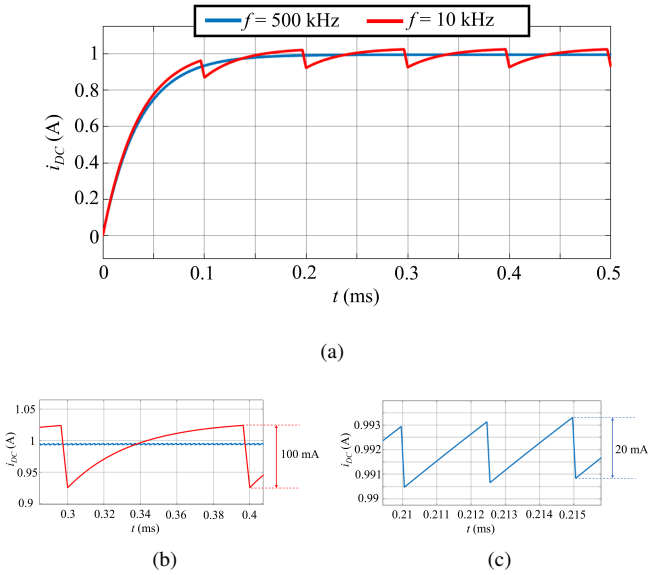

(a) (b) (c)

Fig. 7. Simulated transient behaviour of the magnetizing current, with two different switching frequencies of the DC-DC converter. (a) Comparison of the two switching frequencies. (b) 10 kHz. (c) 500 kHz.

In Fig. 8 the power losses of the current regulator at $f_{\mathrm{s}} = 500$ kHz for different operating current are reported. The main power quote is dissipated on the parasitic resistance of the winding (P_{RDC}). Thanks to the use of GaN power switches, both the conduction (P_{CON}) and switching losses (P_{SW}) are limited.

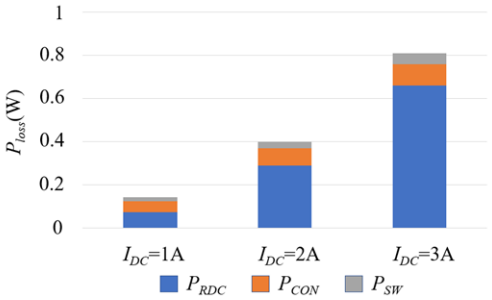

Fig. 8. Power losses of the auxiliary circuit for different operating current values.

V. Experimental Results

The experimental setup is shown in Fig. 9, while in Fig. 10 the voltage across the inductor L_{in} and the voltage across C_{r} are shown. The obtained efficiency and output power results are summarised in Fig. 11, under different magnetizing current I_{DC}. The obtained results confirm the possibility of regulating the output power by controlling the current I_{DC}, and maintaining high conversion efficiency.

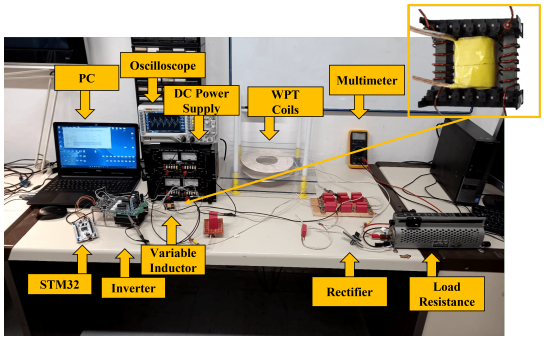

Fig. 9. Photo of the experimental setup with a detail of the controlled variable inductor prototype.

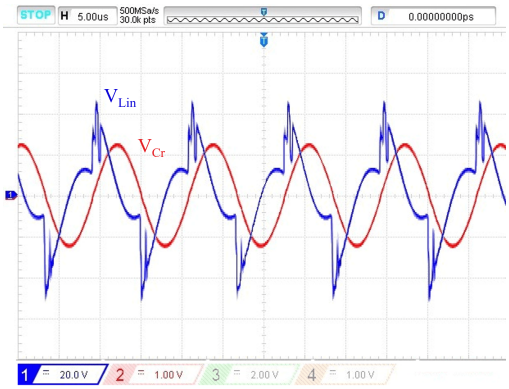

Fig. 10. Measurements of the voltage across the variable inductor L_{in} and voltage across the resonant capacitor C_{r}. The inductor operates in the saturated condition. $V_{\mathrm{L_{in}}} = 20$ V/div, $V_{\mathrm{C_r}} = 1$ V/div, $t = 5$ μs/div

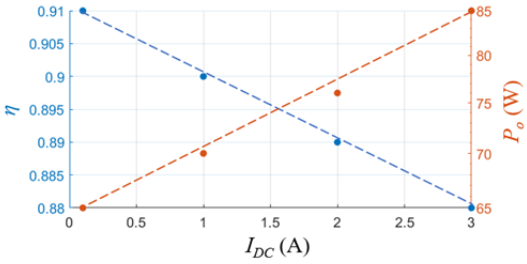

Fig. 11. Measured output power P_{o} and efficiency η of the tested prototype.

VI. Conclusions

In this paper, an LCC-S compensated WPT system regulated by a controlled variable inductor has been presented. A design procedure of the variable inductor according to the system constraints is proposed. Different auxiliary circuits for the DC current regulation have been compared. A switching regulator is proposed, and the additional power losses have been evaluated. The output power and the efficiency of the

whole system have been evaluated for different DC current values.

REFERENCES

[1] S. A. Q. Mohammed and J.-W. Jung, "A Comprehensive State-of-the-Art Review of Wired/Wireless Charging Technologies for Battery Electric Vehicles: Classification/Common Topologies/Future Research Issues," *IEEE Access*, vol. 9, pp. 19 572–19 585, 2021.

[2] F. Corti, A. Reatti, A. Nepote, L. Pugi, M. Pierini, L. Paolucci, F. Grasso, E. Grasso, and M. Nienhause, "A Secondary-Side Controlled Electric Vehicle Wireless Charger," *Energies*, vol. 13, no. 24, p. 6527, Jan. 2020. [Online]. Available: https://www.mdpi.com/1996-1073/13/24/6527

[3] E. Locorotondo, F. Corti, L. Pugi, L. Berzi, A. Reatti, and G. Lutzemberger, "Design of a Wireless Charging System for Online Battery Spectroscopy," *Energies*, vol. 14, no. 1, p. 218, Jan. 2021. [Online]. Available: https://www.mdpi.com/1996-1073/14/1/218

[4] V. Cirimele, M. Diana, F. Freschi, and M. Mitolo, "Inductive Power Transfer for Automotive Applications: State-of-the-Art and Future Trends," *IEEE Transactions on Industry Applications*, vol. 54, no. 5, pp. 4069–4079, Sep. 2018.

[5] W. Xu, W. Liang, J. Peng, Y. Liu, and Y. Wang, "Maximizing Charging Satisfaction of Smartphone Users via Wireless Energy Transfer," *IEEE Transactions on Mobile Computing*, vol. 16, no. 4, pp. 990–1004, Apr. 2017.

[6] E. S. Lee, B. G. Choi, M. Y. Kim, and S. H. Han, "Optimal Number of Turns Design of the IPT Coils for Laptop Wireless Charging," *IEEE Access*, vol. 9, pp. 19 548–19 561, 2021.

[7] P. K. Chittoor, B. Chokkalingam, and L. Mihet-Popa, "A Review on UAV Wireless Charging: Fundamentals, Applications, Charging Techniques and Standards," *IEEE Access*, vol. 9, pp. 69 235–69 266, 2021. [Online]. Available: https://ieeexplore.ieee.org/document/9420719/

[8] L. Pugi, A. Reatti, and F. Corti, "Application of Wireless Power Transfer to Railway Parking Functionality: Preliminary Design Considerations with Series-Series and LCC Topologies," *Journal of Advanced Transportation*, vol. 2018, pp. 1–14, Dec. 2018. [Online]. Available: https://www.hindawi.com/journals/jat/2018/8103140/

[9] Y. Zhang, S. Chen, X. Li, and Y. Tang, "Design of high-power static wireless power transfer via magnetic induction: An overview," *CPSS Transactions on Power Electronics and Applications*, vol. 6, no. 4, pp. 281–297, Dec. 2021.

[10] M. Z. Erel, K. C. Bayindir, M. T. Aydemir, S. K. Chaudhary, and J. M. Guerrero, "A Comprehensive Review on Wireless Capacitive Power Transfer Technology: Fundamentals and Applications," *IEEE Access*, vol. 10, pp. 3116–3143, 2022.

[11] L. Solimene, F. Corti, S. Musumeci, A. Reatti, and C. Ragusa, "Extended ZVS/ZCS operation of Class-E Inverter for Capacitive Wireless Power Transfer," in *2022 IEEE International Conference on Environment and Electrical Engineering and 2022 IEEE Industrial and Commercial Power Systems Europe (EEEIC / I&CPS Europe)*. Prague, Czech Republic: IEEE, Jun. 2022, pp. 1–6. [Online]. Available: https://ieeexplore.ieee.org/document/9854655/

[12] J. Dai and D. C. Ludois, "A Survey of Wireless Power Transfer and a Critical Comparison of Inductive and Capacitive Coupling for Small Gap Applications," *IEEE Transactions on Power Electronics*, vol. 30, no. 11, pp. 6017–6029, Nov. 2015.

[13] F. Corti, A. Reatti, Y.-H. Wu, D. Czarkowski, and S. Musumeci, "Zero Voltage Switching Condition in Class-E Inverter for Capacitive Wireless Power Transfer Applications," *Energies*, vol. 14, no. 4, p. 911, Jan. 2021. [Online]. Available: https://www.mdpi.com/1996-1073/14/4/911

[14] S. Jayalath and A. Khan, "Design, Challenges, and Trends of Inductive Power Transfer Couplers for Electric Vehicles: A Review," *IEEE Journal of Emerging and Selected Topics in Power Electronics*, vol. 9, no. 5, pp. 6196–6218, Oct. 2021.

[15] L. Pugi, A. Reatti, and F. Corti, "Application of modal analysis methods to the design of wireless power transfer systems," *Meccanica*, vol. 54, no. 1, pp. 321–331, Jan. 2019. [Online]. Available: https://doi.org/10.1007/s11012-018-00940-x

[16] X. Lu, P. Wang, D. Niyato, D. I. Kim, and Z. Han, "Wireless Charging Technologies: Fundamentals, Standards, and Network Applications," *IEEE Communications Surveys & Tutorials*, vol. 18, no. 2, pp. 1413–1452, 2016.

[17] K. Onai and O. Ojo, "Performance Analysis and Design of Frequency Controlled Series-Series Compensated Inductive Power Transfer System for Electric Vehicle battery Charging," in *2020 IEEE Industry Applications Society Annual Meeting*, Oct. 2020, pp. 1–8, iSSN: 2576-702X.

[18] V. Cirimele, S. G. Rosu, P. Guglielmi, and F. Freschi, "Performance evaluation of wireless power transfer systems for electric vehicles using the opposition method," in *2015 IEEE 1st International Forum on Research and Technologies for Society and Industry Leveraging a better tomorrow (RTSI)*, Sep. 2015, pp. 546–550.

[19] W. Zhang and C. C. Mi, "Compensation Topologies of High-Power Wireless Power Transfer Systems," *IEEE Transactions on Vehicular Technology*, vol. 65, no. 6, pp. 4768–4778, Jun. 2016.

[20] F. Corti, L. Paolucci, A. Reatti, F. Grasso, L. Pugi, N. Tesi, E. Grasso, and M. Nienhaus, "A Comprehensive Comparison of Resonant Topologies for Magnetic Wireless Power Transfer," in *2020 IEEE 20th Mediterranean Electrotechnical Conference (MELECON)*, Jun. 2020, pp. 582–587, iSSN: 2158-8481.

[21] Y. Chen, H. Zhang, S.-J. Park, and D.-H. Kim, "A Switching Hybrid LCC-S Compensation Topology for Constant Current/Voltage EV Wireless Charging," *IEEE Access*, vol. 7, pp. 133 924–133 935, 2019.

[22] J. Yang, X. Zhang, K. Zhang, X. Cui, C. Jiao, and X. Yang, "Design of LCC-S Compensation Topology and Optimization of Misalignment Tolerance for Inductive Power Transfer," *IEEE Access*, vol. 8, pp. 191 309–191 318, 2020.

[23] W. Wang, J. Deng, D. Chen, Z. Wang, and S. Wang, "A Novel Design Method of LCC-S Compensated Inductive Power Transfer System Combining Constant Current and Constant Voltage Mode via Frequency Switching," *IEEE Access*, vol. 9, pp. 117 244–117 256, 2021. [Online]. Available: https://ieeexplore.ieee.org/document/9514598/

[24] Y. Wei, Q. Luo, and A. Mantooth, "Comprehensive analysis and design of LLC resonant converter with magnetic control," *CPSS Transactions on Power Electronics and Applications*, vol. 4, no. 4, pp. 265–275, Dec. 2019.

[25] Y. Wei, Q. Luo, X. Du, N. Altin, J. M. Alonso, and H. A. Mantooth, "Analysis and Design of the LLC Resonant Converter With Variable Inductor Control Based on Time-Domain Analysis," *IEEE Transactions on Industrial Electronics*, vol. 67, no. 7, pp. 5432–5443, Jul. 2020.

[26] L. Solimene, F. Corti, S. Musumeci, C. S. Ragusa, and A. Reatti, "Magnetic Control of LCC-S Compensated Wireless Power Transfer System," in *2022 International Symposium on Power Electronics, Electrical Drives, Automation and Motion (SPEEDAM)*. Sorrento, Italy: IEEE, Jun. 2022, pp. 160–165. [Online]. Available: https://ieeexplore.ieee.org/document/9842241/

[27] S. Musumeci, L. Solimene, and C. S. Ragusa, "Identification of DC Thermal Steady-State Differential Inductance of Ferrite Power Inductors," *Energies*, vol. 14, no. 13, p. 3854, Jan. 2021. [Online]. Available: https://www.mdpi.com/1996-1073/14/13/3854

[28] N. Wang, Z. Zhang, B. Han, Z. Li, and Y. Lu, "A 250 mA high-precision DC current source with improved stability for the Joule Balance at NIM," in *29th Conference on Precision Electromagnetic Measurements (CPEM 2014)*, Aug. 2014, pp. 644–645, iSSN: 2160-0171.

[29] N. Wang, Y. Zhang, Z. Li, and Z. Zhang, "A DCCT-based 100-A DC current source with high stability," in *2016 Conference on Precision Electromagnetic Measurements (CPEM 2016)*, Jul. 2016, pp. 1–2, iSSN: 2160-0171.

[30] E. Armando, F. Fusillo, S. Musumeci, and F. Scrimizzi, "Low Voltage Trench-Gate MOSFETs for High Efficiency Auxiliary Power Supply Applications," in *2019 International Conference on Clean Electrical Power (ICCEP)*. Otranto, Italy: IEEE, Jul. 2019, pp. 165–170. [Online]. Available: https://ieeexplore.ieee.org/document/8890217/

[31] V. Barba, L. Solimene, M. Palma, S. Musumeci, C. S. Ragusa, and R. Bojoi, "Modelling and Experimental Validation of GaN Based Power Converter for LED Driver," in *2022 IEEE International Conference on Environment and Electrical Engineering and 2022 IEEE Industrial and Commercial Power Systems Europe (EEEIC / I&CPS Europe)*. Prague, Czech Republic: IEEE, Jun. 2022, pp. 1–6. [Online]. Available: https://ieeexplore.ieee.org/document/9854660/